Pulse decomposition analysis in photoplethysmography imaging

Vincent Fleischhauer[1], **Nora Ruprecht**[2], **Michele Sorelli**[3], **Leonardo Bocchi**[3] **and Sebastian Zaunseder**[1]

[1] University of Applied Sciences and Arts Dortmund, Dortmund, Germany
[2] Otto Bock Healthcare Products GmbH, Vienna, Austria
[3] University of Florence, Florence, Italy

E-mail: vincent.fleischhauer@fh-dortmund.de

Keywords: photoplethysmography imaging, pulse wave decomposition, camera, perfusion, remote sensing

Abstract

Objective: Photoplethysmography imaging (PPGI) has gained immense attention over the last few years but only a few works have addressed morphological analysis so far. Pulse wave decomposition (PWD), i.e. the decomposition of a pulse wave by a varying number of kernels, allows for such analyses. This work investigates the applicability of PWD algorithms in the context of PPGI. *Approach*: We used simulated and experimental data to compare various PWD algorithms from the literature regarding their robustness against noise and motion artifacts while preserving morphological information as well as regarding their ability to reveal physiological changes by PPGI. *Main results*: Our experiments prove that algorithms that combine Gamma and Gaussian distributions outperform other choices. Further, algorithms with two kernels exhibit the highest robustness against noise and motion artifacts (improvement in $\overline{\text{NRMSE}}$ of 14.09 %) while preserving the morphology similarly to algorithms using more kernels. Lastly, we showed that PWD can reveal physiological changes upon distal stimuli by PPGI. *Significance*: This work proves the feasibility of pulse decomposition analysis in PPGI, particularly for algorithms with a low number of kernels, and opens up novel applications for PPGI. Not only for PPGI but for future research on PWD in general, our findings have importance as they elucidate differences between PWD algorithms and emphasize the importance of using initial values. To support such future research, we have released the algorithms and simulated data to the public.

1. Introduction

Photoplethysmography (PPG) captures blood volume changes in the microvascular bed of tissue. The technique allows one to capture heart rate and respiration and, most importantly, provides a non-invasive means to determine the arterial oxygen saturation (pulse oximetry), which makes it clinically indispensable (Allen 2007). However, even beyond such measures, PPG signals hold valuable information as the photoplethysmographic waveform reflects the cardiac ejection and the vascular state (Lopez-Beltran *et al* 1998). Various works have related the PPG waveform and its variations to the vasculature in general (vascular age) (Takazawa *et al* 1998, Bortolotto *et al* 2000, Baek *et al* 2007, Chellappan *et al* 2008, Huotari *et al* 2011, Sorelli *et al* 2018), to dynamic cardiovascular parameters (e.g. cardiac output (Wang *et al* 2009) and blood pressure (Padilla *et al* 2009, Wang *et al* 2009, Goswami *et al* 2010)), and to the activity of the autonomous nervous system (ANS) (e.g. ANS activation upon cold stress (Jaryal *et al* 2009, Njoum and Kyriacou 2013, Budidha and Kyriacou 2019)). To analyze the PPG waveform, three approaches are commonly used:

(1) Direct analysis of the PPG waveform (e.g. the alternating component (AC)) (Awad *et al* 2001, Jaryal *et al* 2009, Njoum and Kyriacou 2013, Budidha and Kyriacou 2019).
(2) Analysis of the second derivative of the PPG signal, the so-called acceleration photoplethysmogram (aPPG) (Imanaga *et al* 1998, Takazawa *et al* 1998, Bortolotto *et al* 2000, Iketani *et al* 2000, Miyai *et al* 2001, Hashimoto *et al* 2002, Otsuka *et al* 2006, Baek *et al* 2007, Elgendi *et al* 2010, Huotari *et al* 2011, Elgendi 2012, Inuma *et al* 2012, Xing *et al* 2019) (see figure 1).

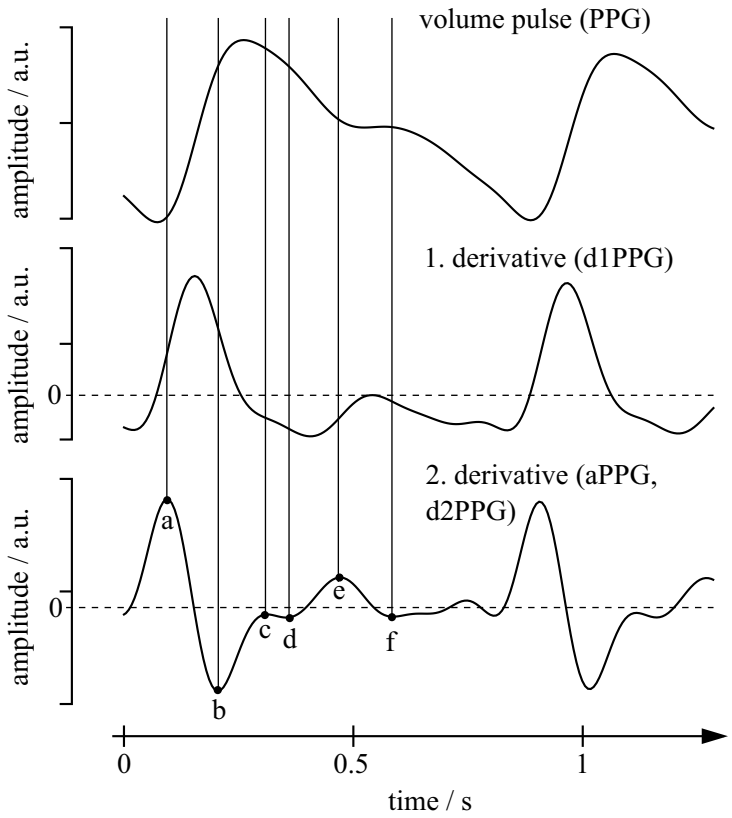

Figure 1. Depiction of a typical PPG waveform and its first and second derivative. Marked in the aPPG are the characteristic waves, *a* to *f*.

(3) Analysis by pulse wave decomposition (PWD), i.e. the fitting of distributions to the PPG waveform and subsequent analysis of fitted distributions (Rubins 2008, Goswami *et al* 2010, Huotari *et al* 2011, Couceiro *et al* 2012, Wang *et al* 2013, Couceiro *et al* 2015, Huang *et al* 2015, Tigges *et al* 2017a, Tigges *et al* 2017b, Sorelli *et al* 2018, Wang *et al* 2018) (see figure 2).

Over the last few years, PPG imaging (PPGI) has gained immense attention. As in conventional PPG, PPGI exploits blood volume changes to derive a pulsatile signal. Instead of using a sensor attached to the skin, PPGI works remotely and uses a camera as sensor (Huelsbusch and Blazek 2002). Most works on PPGI focus on the extraction of the heart rate (HR) and heart rate variability (HRV) (Wang *et al* 2017, Zaunseder *et al* 2018b). However, similar to the conventional PPG waveform, the PPGI waveform can be assumed to feature more information. Only a few works have used morphological analysis to capture this information so far (Trumpp *et al* 2016, Kamshilin *et al* 2017, Trumpp *et al* 2017, Fleischhauer *et al* 2019, Djeldjli *et al* 2019, Nishidate *et al* 2019, Paul *et al* 2019). These works mostly analyzed the amplitude of single pulses, with the exception of the works of Paul *et al* (2019) and Djeldjli *et al* (2019), which employed more complex pulse wave analysis features. As stated before, the second derivative and PWD allow for a much more detailed analysis. However, to the best of our knowledge only Sorelli *et al* (2019) have employed PWD in the context of PPGI. In fact, the application of PWD algorithms to PPGI recordings is troublesome because such recordings typically show a much lower signal-to-noise ratio than conventional signals subject to PWD analyses.

This work investigates the applicability of PWD algorithms in the context of PPGI. Thereto, the aim of the work is twofold. Firstly, we aim to compare various PWD algorithms from the literature. Other than previous works, we not only assess the algorithms' ability to preserve pulse shapes but analyze their robustness to various noise types. Secondly, we apply PWD algorithms to PPGI recordings in order to reveal the benefit of PWD analysis of PPGI recordings.

The remainder of the work is structured as follows. Section 2 gives an overview on existing PWD algorithms and their usage. Section 3 introduces the used data (simulated and real data) and applied methods. Methods cover the general processing of PPGI waveforms, details on used PWD algorithms as well as the applied statistics. Section 4 presents the results on the simulated and experimental data. Section 5 discusses the results and relates them to works from the literature. Finally, in section 6 we provide an outlook for future works.

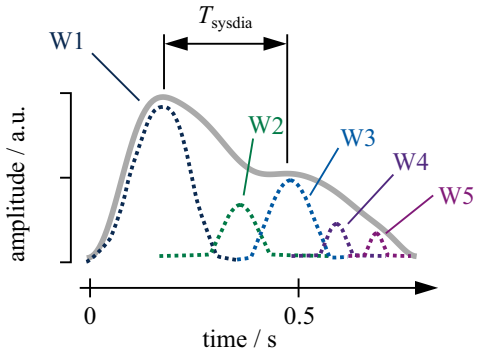

Figure 2. Example for a PWD of the PPG waveform into five Gaussian kernels. T_{sysdia}, as an example of a parameter of the temporal differences of PWD kernels, marks the time interval between the systolic and diastolic components.

2. Background on morphological PPG signal analysis by PWD

PWD assumes that the left ventricular ejection travels through the vascular tree and is reflected at sites where the arterial resistance changes significantly. The pulse waveform, thus, consists of the forward-travelling pulse and several reflections and re-reflections. Pulse decomposition analysis (PDA) is based on the fitting of distributions (so-called basis functions) to the pulse waveform in order to decompose the signal into its basic components (Baruch *et al* 2011, Couceiro *et al* 2015).

PWD is a technique that has been used to decompose pulse waves into a varying number of basic components (kernels). From the relationship between these kernels several PWD parameters can be derived (see table 1 for a list of works regarding PWD algorithms and their usage). The derived parameters comprise mainly temporal differences and amplitude ratios of the kernels. They have been associated with aging and arterial stiffening, pulse wave velocity, blood pressure and sympathetic activation (Rubins 2008, Goswami *et al* 2010, Baruch *et al* 2011, Couceiro *et al* 2012, Baruch *et al* 2014, Liu *et al* 2014, Couceiro *et al* 2015, Wang *et al* 2018, Sorelli *et al* 2018, Sorelli *et al* 2019).

Besides analyzing parameters of the decomposition, PWD can be used to preprocess distorted data. Couceiro *et al* (2012, 2015) and Lazaro *et al* (2018) have used PWD to reduce the noise in PPG recordings. This opens up the possibility to analyze the derivatives of noisy PPG signals. This is an interesting approach as PPGI signals usually show a bad signal-to-noise ratio (SNR) in comparison to conventional PPG.

As can be seen in table 1, there is a wide variety of suggested PWD algorithms in the literature that differ in the number and type of used kernels. Tigges *et al* (2017a) conducted a comparison of accuracy between several PWD algorithms and found an algorithm based on three Gamma kernels to achieve the best results. Huang *et al* (2015) examined the benefit of the usage of a mixture of Gamma and Gaussian kernels over pure Gaussian kernel-based algorithms and showed that the algorithm consisting of a Gamma kernel and three Gaussian kernels exhibited the best results in residual analysis. Liu *et al* (2013) showed that models with three Gaussian kernels achieve a better modeling accuracy than models with fewer kernels. A quantitative analysis of the suitability of algorithms is difficult as only a few works have evaluated the differences between such algorithms extensively and the results differ (Liu *et al* 2013, Huang *et al* 2015, Tigges *et al* 2017a).

3. Methods and materials

3.1. Data

3.1.1. Simulated data

In order to compare the implemented PWD algorithms in terms of robustness, we used simulated PPG data. For each class of the PPG according to Dawber *et al* (1973) we modeled a single beat of a PPG (see figure 3(a)–(d)). To that end, we decomposed real PPG beats of the respective class by each decomposition algorithm. We inspected the decompositions visually to make sure that the reconstructed beats matched the original real PPG beat. We then added noise to these templates (see figure 3(e)–(h)). We used white and pink noise as well as motion artifacts with the SNR ranging from 10 dB to 100 dB. While modeling white and pink noise is straightforward, there is no standard procedure to model motion artifacts. Appendix B contains the details on such modeling. The SNR is defined as the quotient of the signal energy and the noise power spectral density. Notably, the modeling made use of the respective algorithm under consideration, i.e. an

Table 1. Works regarding PWD. Note that some of these works do not use PWD to assess the PPG waveform, but rather continuous blood pressure signals. Appendix A explains the abbreviations of the PWD features listed in this table. (+) denotes a statistically significant positive correlation, (-) a negative one.

work	PWD kernels	Research object/PWD features	Physiological correlation
(Rubins 2008)	4 Gaussian	AuI and RI	
(Goswami *et al* 2010)	2 Rayleigh	RI, DPS	BP (+)[(1)]
		T12, D	BP (-)
(Baruch *et al* 2011)[(a)]	Not specified	T13	BP (+), BBI (+)[(2)]
(Huotari *et al* 2011)	5 Log-Normal	Analysis of residuals	
		AgI	Vascular age
(Couceiro *et al* 2012)	4 Gaussian	Estimation of LVET[(3)]	
(Liu *et al* 2013)[(a)]	1 to 3 Gaussian	Model comparison	
(Wang *et al* 2013)	4 to 5 Gaussian (adaptive)	Model presentation	
(Baruch *et al* 2014)[(a)]	Not specified	T13	Central PP (+)[(4)]
		P2P1	Central systolic BP (+)
(Liu *et al* 2014)[(a)]	3 Gaussian	T12	Systolic BP (-)
		P2P1	Systolic blood pressure (+)
(Huang *et al* 2015)	2 to 5 Gaussian, Gamma and Gaussian	Analysis of residuals, Model comparison	
(Couceiro *et al* 2015)	5 Gaussian	RI, SI, T12, T1d, R12, R1d	Systolic BP (+), diastolic BP (+), mean BP (+), PP (+), TPRI (+)[(5)]
			Estimation of LVET
(Banerjee *et al* 2017)	2 Gaussian	T12	Mental stress (+)
(Tigges *et al* 2017a)	1 to 6 Gaussian, log-normal, Rayleigh, Gamma	Model comparison	
(Tigges *et al* 2017b)	3 Gamma	Shows applicability of PWD to in-ear PPG recordings	
(Wang *et al* 2018)	3 Gaussian	T12, T13, P2P1	Exercise (+)
		P3P1	Exercise (-)
(Sorelli *et al* 2018)[(b)]	4 Gaussian	Modified SI and RI, CT, T12, T13, T14, P2P1, P3P1 and P4P1 used to estimate vascular age	
(Lazaro *et al* 2018)	2 Gaussian	T12	Estimation of respiratory rate
(Sorelli *et al* 2019)	4 Gaussian	T12, T13, T14, CT	Cold stimulus (+)
		SI	Cold stimulus (-)
		RI	

[(1)] Blood pressure (BP),[(2)] beat-to-beat intervals (BBI),[(3)] left ventricular ejection time (LVET),[(4)] pulse pressure (PP),[(5)] total peripheral resistance index (TPRI).

[(a)] Analysis of continuous blood pressure signals,[(b)] analysis of laser Doppler flowmetry signals.

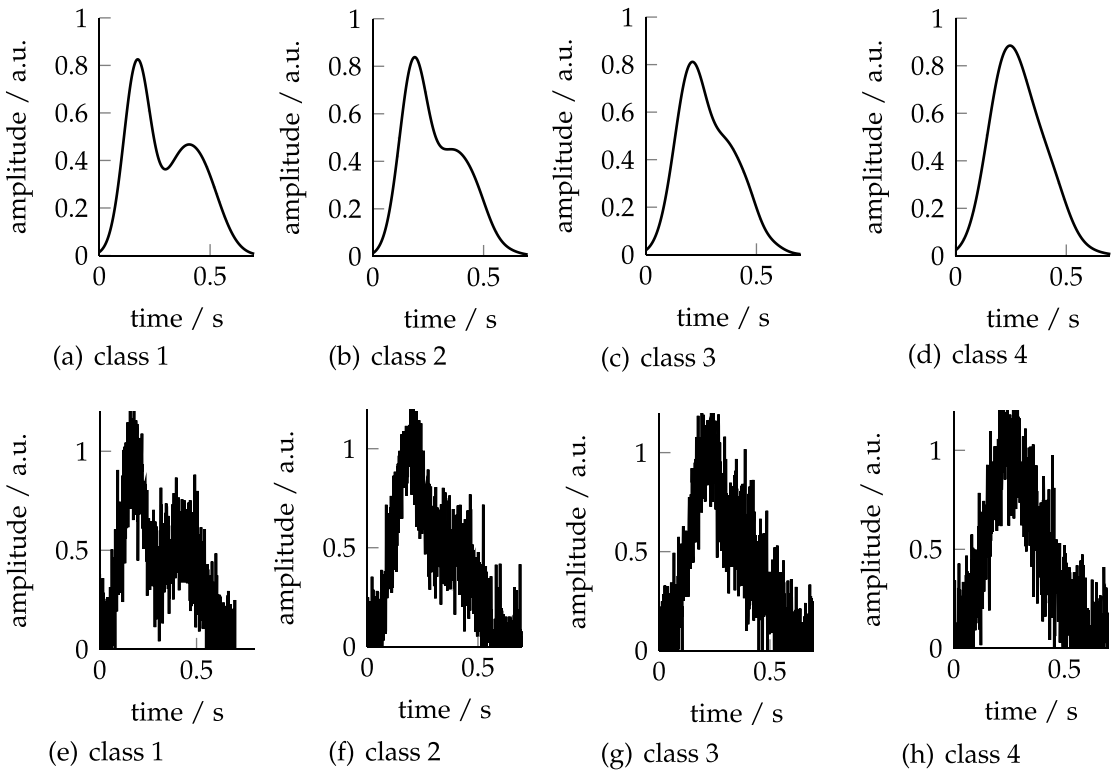

Figure 3. Depiction of the Dawber classes of the PPG waveform. While class 1 exhibits a clearly visible incisura, which separates the systolic and diastolic components, the incisura becomes less pronounced with increasing class. In class 4, systole and diastole cannot be distinguished (Dawber *et al* 1973). Also depicted is this set of templates superimposed with white noise. The SNR of these signals is 10 dB.

algorithm that uses three kernels is evaluated by beats simulated by three kernels as well. This procedure ensures that the simulated data allow assessment of the robustness against noise.

3.1.2. Experimental data

On the one hand, we used experimental data, namely finger PPG, to assess the model quality, i.e. the ability to preserve the morphology by various algorithms. On the other hand, we used experimental data, namely PPGI recordings, for physiological considerations. The dataset used in this analysis originates from a so-called cold pressure test (CPT). The CPT provokes cold pain and thus elicits a sympathetic response (Skoluda *et al* 2015). We used an RGB camera (UI-3370CP-C-HQ, IDS) with a color depth of 12 bits, a frame rate of 100 fps and a resolution of 420 × 320 pixels for video recordings of the face. The experimental setup was illuminated by ambient light and a fluorescent ceiling light. Non-invasive continuous blood pressure (Finometer Midi, Finapres Medical Systems), PPG, electrocardiography and respiration signals (all sensors from ADInstruments) were recorded as reference data.

The experiment overall lasted approximately 11 min and included resting phases and a CPT. Our analysis focuses on five analysis intervals of 10 s each. At the beginning, participants executed a resting phase of 480 s. From this phase, three baseline measurements were taken (*Baseline 1* to *3*). After that, the CPT started by immersing one hand into cold water with a constant temperature of 3 °C. The stimulus lasted up to 3 min. The participants were free to quit stimulation earlier. Two more analysis intervals were defined at the time interval 10 s after the start of the stimulation (*AfterCPT*) and the time interval 5 s before and after the time instant at which the systolic blood pressure reached its peak value (*HighestSBP*). The response to the CPT shows an individual time course. We assessed *HighestSBP* as we assume the physiological impact of the CPT to be most pronounced independently from its temporal occurrence. *AfterCPT*, on the other hand, shows the immediate physiological response to the CPT.

A total of 22 healthy subjects (age 25.5 ± 3.73 years, 10 female) participated in the study. Each participant took part twice, once in supine position and once in sitting position. As a consequence of the varying recording positions and their temporal separation, different recordings of the same subject were considered independent. One recording had to be discarded due to technical problems. The study has been approved by the institutional review board of TU Dresden (EK119 032 016). All participants were informed about the experimental procedure and gave written consent.

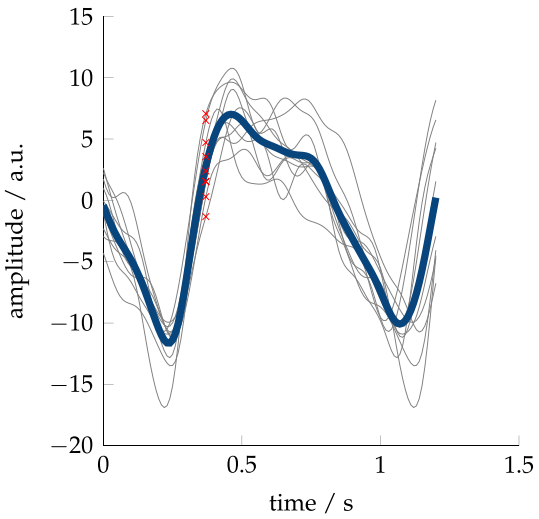

Figure 4. Exemplifying template generation by ensemble averaging. Single beat segments are shown in light gray with their respective beat detections t_i marked with red crosses. The resulting template is shown in bold dark blue.

3.2. Preprocessing of experimental data

In our analyses, we only used the green channel of the video recordings as it provides the highest signal quality (Verkruysse *et al* 2008). Each pixel of a frame within a manually defined region of interest (ROI) on the forehead was then averaged to obtain a single pixel trace per video. Furthermore, the pixel traces were bandpass filtered by applying a fifth-order Butterworth filter of cutoff frequency 8 Hz and a third-order Butterworth filter of cutoff frequency 0.4 Hz, in forward and backward direction, respectively, and subtracting their outputs to yield the filtered PPGI signal. We used the algorithm of Lazaro *et al* (2014) in order to detect single pulses in the 10 s analysis intervals. Around each beat detection t_i, we defined a beat segment as

$$\text{start}_{\text{beat}} = t_i - 0.45 \cdot \widetilde{\text{BBI}}_{\text{PPGI}}$$

$$\text{end}_{\text{beat}} = t_i + \widetilde{\text{BBI}}_{\text{PPGI}}\,, \tag{1}$$

where $\widetilde{\text{BBI}}_{\text{PPGI}}$ denotes the median interval of all beat-to-beat intervals in the respective analysis interval. We discarded beat segments if $\text{start}_{\text{beat}}$ or end_{beat} were located outside the analysis interval or if they showed a mean correlation to all segments lower than 0.3. The remaining pulses were then ensemble averaged, thus obtaining a single beat template for each analysis interval (see figure 4). The reference PPG was filtered and ensemble averaged in the same way (Fleischhauer *et al* 2019).

3.3. Pulse decomposition algorithms

We implemented 19 PWD algorithms using Gaussian and Gamma basis functions as these are the most common basis functions in the literature (see table 1). In the following sections, we describe the implemented algorithms with their respective initial values, boundaries and constraints for optimization. All algorithms use the interior point optimization method from the Matlab function *fmincon* due to its ability to handle both inequality constraints and boundaries. The function uses its default settings, the only exception being the maximum number of function evaluations, which was set to infinite.

3.3.1. Used kernel combinations

This section gives an overview of the definitions of the used kernel combinations. All kernels $g(t, \theta)$ are functions of time t and a parameter vector to be optimized θ. Each parameter vector contains three parameters that adjust the kernels amplitude, location and width. We implemented each kernel combination using two to four kernels as these are typical numbers of used kernels in the literature. The pure Gaussian algorithm was also used with five kernels in order to adapt the algorithm of Couceiro *et al* (2015).

Naming of algorithms indicates kernel combination (Gaussian, Gamma, GammaGaussian) followed by the number of kernels (2, 3, 4, 5). The last part consists of the method for obtaining the initial values and boundaries (Couceiro, Sorelli, generic).

Gaussian
The most commonly used kernel is the Gaussian distribution (see table 1). The probability density of the Gaussian distribution can be written as (Rubins 2008):

$$g_{\text{Gaussian},k}(t,\theta_k) = a_k \cdot e^{\frac{-(t-\mu_k)^2}{2\sigma_k^2}}, \tag{2}$$

where θ_k denotes the k-th parameter vector that consists of the amplitude a, the mean μ and the standard deviation σ. The Gaussian algorithms decompose the pulse wave into a number of N Gaussian kernels; the reconstructed signal y can thus be defined as the sum of the N kernels:

$$y_{\text{Gaussian,N}}(t,\theta) = \sum_{k=1}^{N} g_{\text{Gaussian},k}(t,\theta_k). \tag{3}$$

Gamma
The use of Gamma kernels in PWD was first introduced in the work of Huang *et al* (2015). Like other skewed distributions (e.g. Rayleigh or log-normal) it is used to model the steep slope of the systolic part of the PPG waveform. Moreover, Couceiro *et al* (2012) stated that the central volume pulse is not symmetric. It is thus likely that the peripheral volume pulse is asymmetric as well, and should, therefore, be represented by an asymmetric kernel. The Gamma probability density function in its α/β-parametrization is (Tigges *et al* 2017a):

$$g_{\text{Gamma},k}(t,\theta_k) = \frac{\beta_k^{\alpha_k}}{s_k \cdot \Gamma(\alpha_k)} t^{\alpha_k - 1} e^{-\beta_k t}. \tag{4}$$

Tigges *et al* also made use of Gamma kernels in their works (Tigges *et al* 2017a, Tigges *et al* 2017b). They expressed the shape parameter α and the rate parameter β through the mode m and standard deviation σ for a more convenient and meaningful definition of boundaries for the parameter vector as it is quite difficult to interpret α and β. In equation (4) they also added the parameter s to the regular definition of the Gamma distribution in order to scale the amplitude of the kernel. Appendix C explains the expression used in this work. The parameter vector of the Gamma kernel is thus $\theta = [\sigma, m, a]$. The modeled signal

$$y_{\text{Gamma,N}}(t,\theta) = \sum_{k=1}^{N} g_{\text{Gamma},k}(t,\theta_k) \tag{5}$$

is expressed as a the sum of N Gamma kernels.

Gamma Gaussian
We also implemented a combination of a Gamma kernel and a number of Gaussian kernels as proposed by Huang *et al* (2015), who showed that this combination leads to a better fit than a pure Gaussian model. The kernels are defined as in equation (2) and equation (4). Therefore, the reconstructed signal y from N kernels is defined as

$$y_{\text{GammaGaussian,N}}(t,\theta) = g_{\text{Gamma},1}(t,\theta_1) + \sum_{k=2}^{N} g_{\text{Gaussian},k}(t,\theta_k). \tag{6}$$

3.3.2. Boundaries and initial values
Some works take *a priori* knowledge into account to define the initial values and boundaries for their optimization algorithms (Couceiro *et al* 2015, Banerjee *et al* 2017, Sorelli *et al* 2018). From these algorithms, we implemented the method of Couceiro *et al* (2015), which is the most commonly adapted algorithm, and the method of Sorelli *et al* (2018), which was previously used on PPGI signals. Both methods make use of the signal's derivatives, which might cause problems due to the comparatively low SNR of PPGI recordings and distortions of the morphology due to movement artifacts. We thus also implemented an approach that uses generic initial values and does not restrict the kernels. Appendix D lists the boundaries and initial values of each algorithm in detail.

Method of Couceiro

Couceiro *et al* (2012, 2015) proposed an algorithm that extends the method of Rubins (2008) of analyzing the second derivative of the pulse wave in order to separate the systolic and diastolic components. This extended method also makes use of the third and fourth derivatives. A similar method, which is also based on the second derivative but uses optimization parameters depending on the extended Dawber class [4] of the waveform, is introduced in the work of Wang *et al* (2013). Table D1 shows the initial boundaries and values of the method of Couceiro *et al* (2015). Equation (7) defines the four constraints for their algorithm regarding the amplitude a and the position μ:

$$\begin{aligned} &a_1 - a_2 \leq 0 \wedge a_1 - a_3 \leq 0 \\ &a_3 - a_2 \leq 0 \wedge a_4 - a_2 \leq 0 \wedge a_5 - a_2 \leq 0 \\ &a_5 - a_4 \leq 0 \\ &\quad \mu_1 \leq \mu_2 < \mu_3 \leq \mu_4 \leq \mu_5 \,. \end{aligned} \tag{7}$$

We implemented the algorithm of Couceiro *et al* in its original version from the literature consisting of five Gaussian kernels.

Method of Sorelli

The algorithm of Sorelli *et al* (2018, 2019) is based on the windowing of the pulse into a systolic and a diastolic part. For this purpose, the algorithm assesses the first derivative of the signal. The initial values and boundaries that are derived from the length and the signal amplitude of the systolic and diastolic phase, respectively, are listed in table D2. The algorithm applies the following constraints to the optimization of the position μ:

$$\mu_{k-1} < \mu_k \qquad k \in \{3, \ldots, N\} \,. \tag{8}$$

We implemented the algorithm of Sorelli *et al* (2018, 2019) for all used kernel combinations using two to four kernels except the Gamma4sorelli algorithm (see section 5.1 for an explanation).

Generic values

In this method, the initial parameters and boundary conditions are not determined based on the pulse wave, but follow a generic and simple concept, which distributes the basis functions over the waveform. Table D3 details the used values. These values were applied regardless of the types of kernels. We also defined the following constraints to the amplitude a and the position μ:

$$\begin{aligned} a_1 &> a_k \\ \mu_{k-1} &< \mu_k \qquad k \in \{2, \ldots, N\} \,. \end{aligned} \tag{9}$$

We implemented algorithms with generic values for all used kernel combinations using two to four kernels. For the Gaussian basis functions we also implemented a model consisting of five kernels in order to compare this method to the algorithm of Couceiro *et al* (2015).

3.4. Assessment of model quality

For the comparison, the implemented PWD algorithms decompose the noisy simulated signals and reconstruct the signal by adding the optimized basis functions. The normalized root mean square error (NRMSE) (Liu *et al* 2013, Sorelli *et al* 2018) of the second derivative of the reconstructed signal, $\mathrm{aPPG}_{\mathrm{rec}} = \frac{d^2\mathrm{PPG}_{\mathrm{rec}}(n)}{d\mathrm{n}^2}$, with regard to the second derivative of the undistorted simulated reference template, $\mathrm{aPPG}_{\mathrm{ref}} = \frac{d^2\mathrm{PPG}_{\mathrm{ref}}(n)}{d\mathrm{n}^2}$, is then calculated to assess the goodness of fit:

$$\mathrm{NRMSE} = 1 - \frac{\sqrt{\sum_{n=1}^{N} \left(\mathrm{aPPG}_{\mathrm{ref}}(n) - \mathrm{aPPG}_{\mathrm{rec}}(n)\right)^2}}{\sqrt{\sum_{n=1}^{N} \left(\mathrm{aPPG}_{\mathrm{ref}}(n) - \overline{\mathrm{aPPG}}_{\mathrm{ref}}(n)\right)^2}} \,, \tag{10}$$

where N denotes the number of samples of the simulated signal. Note that though this is a measure of error, the NRMSE attains values in the range of $(-\inf, 1]$, where NRMSE $= 1$ marks a perfect fit. We chose to assess the NRMSE of the second derivative because the second derivative accentuates distortions of the

[4] Wang *et al* (2013) described an additional fifth class of the PPG waveform, thereby extending the Dawber classes.

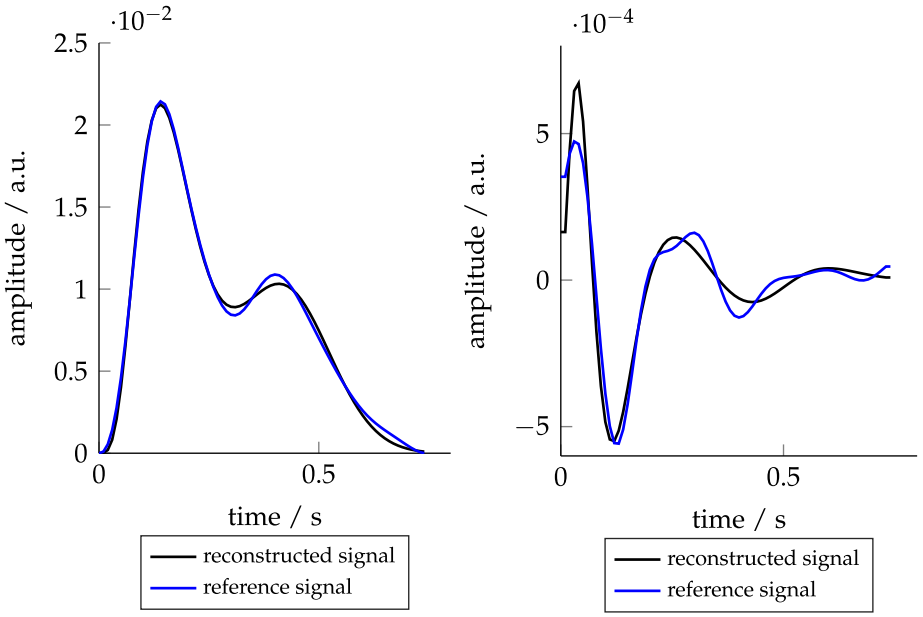

(a) PPG (b) aPPG

Figure 5. Depiction of the decomposition of a reference PPG. The NRMSE of the aPPG is 0.6993. This figure also shows the accentuation of the distortions in the second derivative, as the NRMSE of the PPG is 0.9467.

signal, thus providing a stricter comparison than the original signal (see figure 5). In addition, we also wanted to test the ability of the PWD algorithms to cope with noise because this is essential to successfully evaluate the second derivative of noisy PPGI data. For each algorithm and noise level, we conducted 25 repetitions of the decomposition. In each repetition the noise was generated randomly. For the motion artifacts, we raised the number of repetitions to 250 to account for the increased degrees of freedom.

We also decomposed the ensemble averages of the reference PPG of the baseline analysis intervals with every algorithm. In this way, we could assess the quality of the reconstructed beats on real data in order to evaluate the algorithms' ability to preserve the shape.

3.5. Physiological considerations

We assessed the PPGI data with the algorithm from each kernel number that showed the overall best goodness of fit, i.e. the highest mean NRMSE over all iterations, classes, types of artifact and SNR values. From the decomposed PPGI recordings, we analyzed the resulting kernels as well as the second derivatives of the reconstructed signals. Therefore, we calculated the ratio of the b wave to the a wave of the second derivative b/a and the time between the systolic and diastolic component T_{sysdia}. The T_{sysdia} parameter takes the amplitude a_{mk} at the mode m_k (i.e. the point in time at which the maximum occurs) of the k-th kernel g as well as the number of kernels N into account:

$$T_{\text{sysdia}} = \left(\frac{\sum_{k=2}^{N} a_{\text{mk}} \cdot m_k}{\sum_{k=2}^{N} a_{\text{mk}}} \right) - m_1 \,. \tag{11}$$

For this parameter we assume the first kernel to model the systolic component, while the diastolic component consists of the remaining kernels. From the reference signals, we assessed the median length of the beat-to-beat intervals (BBI) derived from the reference PPG as well as the pulse pressure (PP) as these parameters have been shown to correlate with the T13 parameter (Baruch *et al* 2011).

3.6. Statistical analysis of PPGI recordings

We excluded 10 of the 43 recordings because they contained missing values. For four subjects, the placement of analysis intervals failed or no stable forehead region could be defined. Ensemble averaging failed due to too few beats in the PPGI signal for six subjects. Thus, 33 recordings were analyzed.

The results for each algorithm were assessed independently. We compared three analysis intervals against one another (*Baseline 3*, *AfterCPT* and *HighestSBP*), thereby creating non-orthogonal contrasts. As our CPT dataset consists of 33 subjects, we assumed a normal distribution (WeiB 2013). In order to account for multiple testing, we used a repeated measures ANOVA as an omnibus test and the t-test for paired data as the

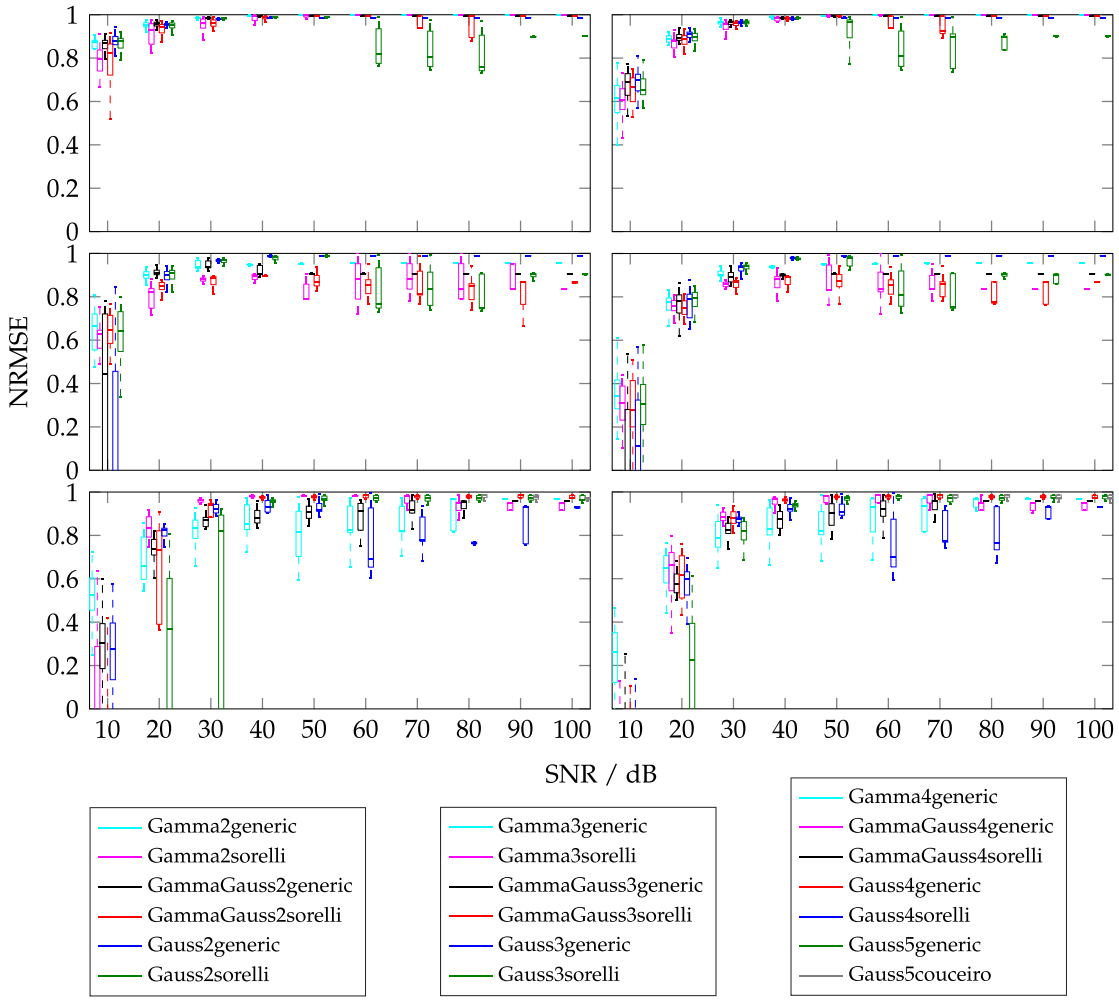

Figure 6. Results of the comparison of the PWD algorithms on the simulated data for white (left column) and pink (right column) noise. Each row shows the results of a set of algorithms: two kernels (top row), three kernels (middle row), four and five kernels (bottom row).

post-hoc test. Furthermore, we used the Holm–Bonferroni correction to counteract multiple comparisons by conducting one Friedman test per dependent variable (Holm 1979). The Holm–Bonferroni correction was also applied to adjust the p values of the post-hoc tests to account for the non-orthogonal contrasts.

4. Results

4.1. Shape preservation

Figure 6 depicts the results of the comparison on the simulated noise data. We found the results regarding white and pink noise to be similar. As is to be expected, the NRMSE generally decreases for lower SNR values. The comparisons of each of the three figures show a worsening of fit with an increasing number of kernels. The results for the simulated movement artifacts are displayed in figure 7 and generally resemble the results on the noisy data. The five-kernel algorithms exhibited the lowest NRMSE. This is especially true for the Gauss5couceiro algorithm, which achieved the overall lowest mean NRMSE of all algorithms ($\overline{\text{NRMSE}} = -10.9393$). The algorithms using fewer kernels showed relatively high NRMSE values. For these algorithms, a rapid decrease of the NRMSE can be observed between 30 dB and 10 dB. The highest mean NRMSE for each number of kernels is achieved by the GammaGauss2generic algorithm ($\overline{\text{NRMSE}} = 0.9497$), the Gamma3generic algorithm ($\overline{\text{NRMSE}} = 0.8324$), the Gamma4generic algorithm ($\overline{\text{NRMSE}} = 0.7553$) and the Gauss5generic algorithm ($\overline{\text{NRMSE}} = -1.0810$). Besides the assessment of the NRMSE, we also extracted the parameters T_{sysdia} and b/a from the simulated data (not shown here). Algorithms with fewer kernels exhibited a more consistent calculation of the parameters, thus supporting our findings from the analysis of the NRMSE.

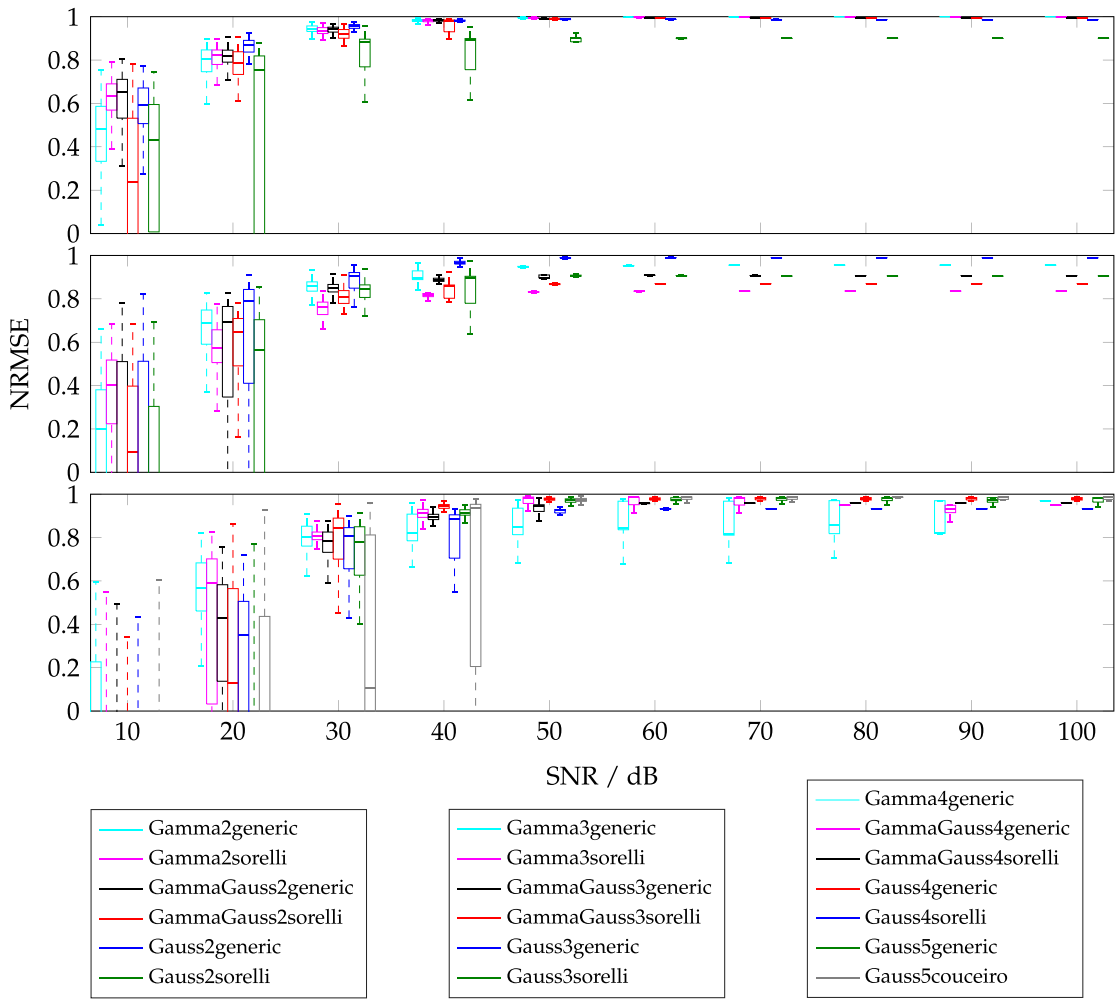

Figure 7. Results of the comparison of the PWD algorithms on the simulated data for movement artifacts. Each row shows the results of a set of algorithms: two kernels (top row), three kernels (middle row), four and five kernels (bottom row).

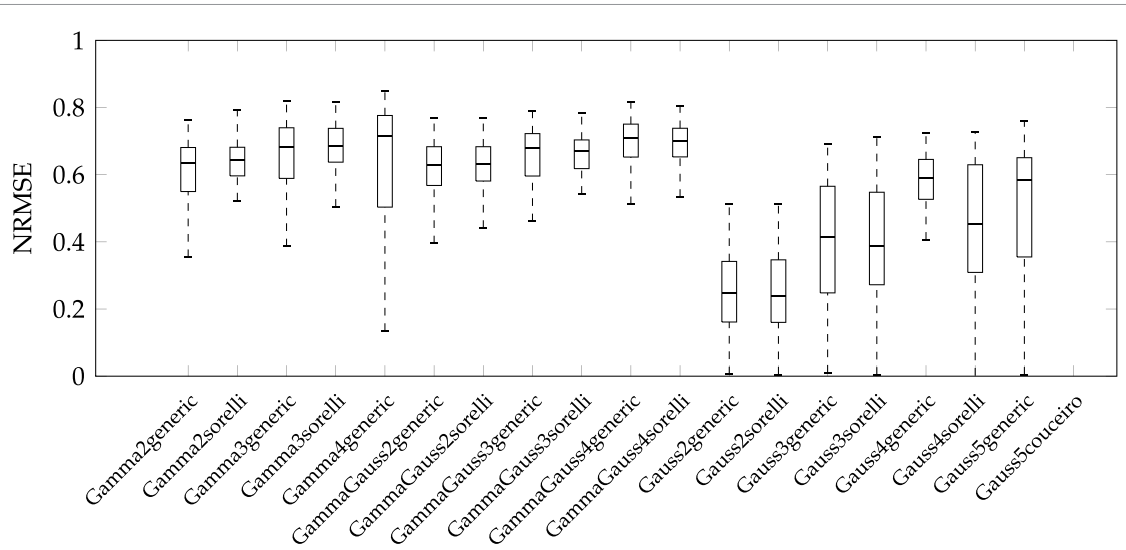

Figure 8. Depiction of the NRMSE of the decomposition of the reference PPG data. The reference data are considered to be noiseless. The 75th percentile of the NRMSE of the Gauss5couceiro algorithm is less than zero and thus not depicted in this plot.

The results of the assessment of the algorithms' shape preservation ability are depicted in figure 8. The algorithms containing Gamma kernels exhibit generally higher mean NRMSE values than the pure Gaussian algorithms. The GammaGauss4generic algorithm achieves the highest mean NRMSE ($\overline{\text{NRMSE}} = 0.6719$).

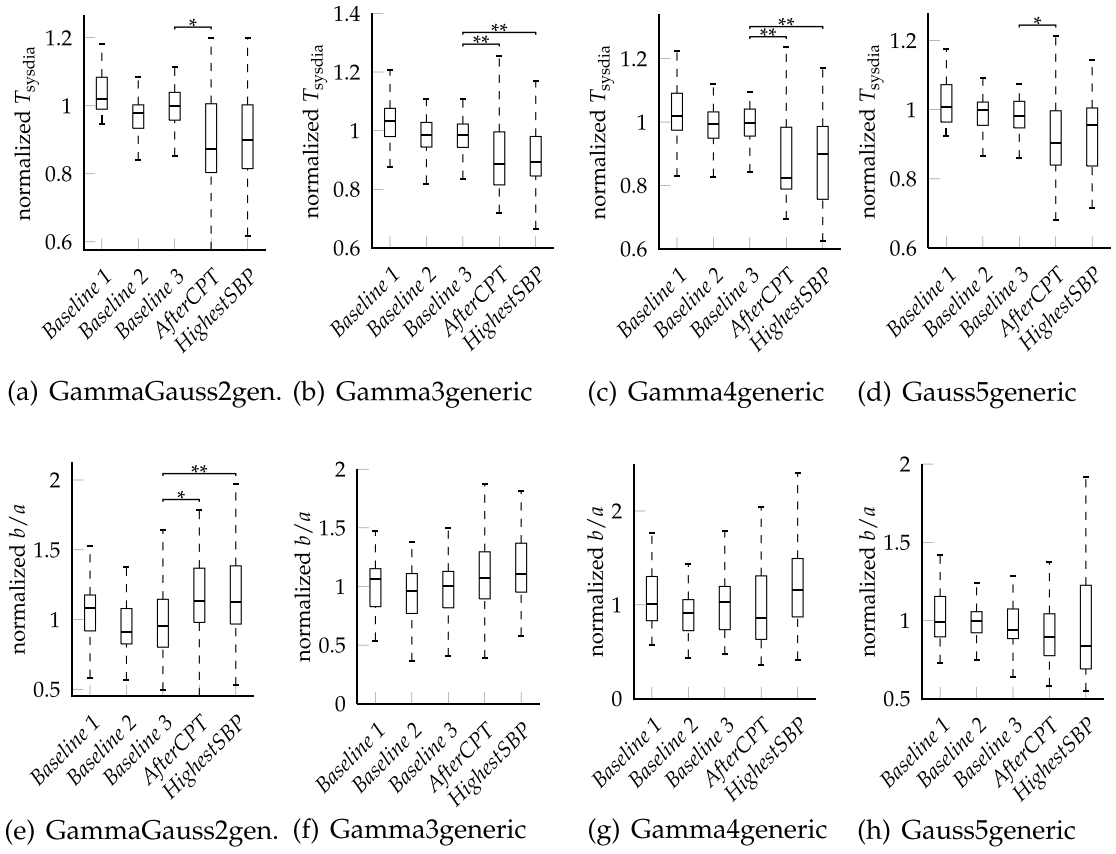

Figure 9. Results of the assessment of the CPT dataset, depicted by boxplots. If significant, post-hoc test outcomes are denoted by * $p < 0.05$, ** $p < 0.01$, *** $p < 0.001$. Outliers are not shown. All values are normalized to the mean of the three baseline analysis intervals.

4.2. Physiological considerations

This section covers the results of the assessed parameters on the CPT dataset. Due to the results in section 4.1, the algorithms achieving the highest mean NRMSE on the simulated data for each number of kernels were applied to the PPGI data for physiological considerations. Figures 9(a) and (e) depict the parameters derived from the GammaGauss2generic algorithm. Both T_{sysdia} and b/a exhibited statistically significant changes between the analysis intervals, with T_{sysdia} showing a significant decrease between *Baseline 3* and *AfterCPT* ($p = 0.0148$). At *HighestSBP* the median T_{sysdia} remained at the level of *AfterCPT*. However, b/a increased after the application of the stimulus, reaching its maximum at *HighestSBP*, where the difference to *Baseline 3* was very significantly different ($p = 0.0069$).

The rest of the plots in figure 9 show the results for the Gamma3generic, Gamma4generic and Gauss5generic algorithms. A statistically significant decrease in T_{sysdia} for all algorithms can be noted. Though not significant, Gamma3generic exhibited a similar trend to the GammaGauss2generic algorithm in the b/a parameter. Gamma4generic did not show a trend, while Gauss5generic demonstrated an opposing trend. In contrast to the GammaGauss2generic algorithm, no algorithm showed any significant difference between the analysis intervals.

5. Discussion

5.1. Model comparison

The simulation showed that the robustness of PWD algorithms against noise and motion artifacts decreased with an increasing number of kernels. This is to be expected, as with an increasing number of kernels, the possibility of the kernels adapting to a distorted waveform rises. No substantial difference could be found between the results for white and pink noise.

A very important finding concerning the algorithms' real use is the impact of initial values and boundary conditions. As can be seen in figure 6, the NRMSE of the algorithm of Couceiro *et al* (2015) suffered a reduction even at high SNR values. This can be explained by the dependency on the second, third and fourth derivatives of the PPG waveform as the derivatives amplify the noise. The algorithm of Sorelli *et al* (2018)

relies on the first derivative, which makes it susceptible to noise as well. This algorithm, however, implements several interceptions that stabilize the decomposition. The generic algorithms are the least affected by noise.

Algorithms containing Gamma kernels achieved overall better NRMSE values than pure Gaussian kernels. This is in accordance with the literature (Huang *et al* 2015, Tigges *et al* 2017b), according to which skewed kernels have been better suited to model the steep slope of the systolic phase of the PPG waveform.

This can also be seen in figure 8, which shows the NRMSE of the decomposition of the reference PPG. The reference data is considered to be noiseless. As there were only minor differences in the shape preservation ability of the algorithms containing Gamma kernels, the comparison showed that algorithms consisting of two kernels were sufficient for PWD.

A drawback of the Gamma kernel is the codomain of the Gamma function. Equation (4) contains the term $\Gamma(\alpha_k)$, where α_k increases with the mode m. For algorithms with a high number of kernels N, for k close to N, $\Gamma(\alpha_k)$ can attain values that exceed the range of a double precision variable, thus being treated as infinity. Due to this, the Gamma4sorelli algorithm could not produce a template for the comparison and was thus not included in this work. This problem could be solved by using other skewed distributions like the Rayleigh or log-normal distribution (Tigges *et al* 2017b).

As table 1 shows, PWD algorithms have been compared before. In contrast to our work, these model comparisons used continuous blood pressure (Liu *et al* 2013) or PPG recordings (Huang *et al* 2015, Tigges *et al* 2017a) to evaluate the goodness of fit of the tested algorithms. As these works aimed to compare the goodness of fit of various algorithms to real signals, while our work additionally included the robustness of algorithms against noise, the results are not directly comparable.

Liu *et al* (2013) compared only pure Gaussian algorithms with one to three kernels. They found three kernels to achieve the best fit. This is to be expected, as a higher number of kernels leads to more degrees of freedom, thus improving the goodness of fit. In our comparison, the NRMSE decreases with the number of kernels as we measure the goodness of fit of the decomposition of the noisy signal to the undistorted signal. It can thus be assumed that algorithms with more than two kernels adapt to the noise.

Huang *et al* (2015) concluded from their comparison that the use of the GammaGaussian kernel combination resulted in a lower mean absolute error than a pure Gaussian model. This corresponds with our observations and can be explained as above.

A model consisting of three Gamma kernels also performed well in the comparison of Tigges *et al* (2017a). As they used the corrected Akaike information criterion (AICc), the number of kernels of an algorithm was penalized, which further complicates comparison to our results in this regard. Nonetheless, our work also suggests that for three basis functions a combination of Gamma kernels achieves the best fit, thus confirming the findings of Tigges *et al* (2017a).

The aforementioned comparisons did not take into account the physiological reasonableness. For example, Tigges *et al* (2017a) used the algorithm of Couceiro *et al* (2015), which considers more than one kernel to model the systolic part of the PPG waveform. Similarly, Wang *et al* (2013) presented a model that used four or five kernels depending on the improvement of the goodness of fit by inserting an additional kernel. This is physiologically questionable, as it would be possible for successive PPG beats to be modeled by a different number of kernels.

5.2. Physiological interpretation of the results

The decomposition of the PPGI data also suffered from physiologically unreasonable results. The constraints of the algorithms allow the amplitude of the diastolic kernels to become zero. This happens especially with the Gauss5generic algorithm. This problem complicates the assessment of ratios of the kernels. It should be noted, though, that the optimal number of kernels remains an issue of dispute in the literature. Some works propose three kernels to cover the crucial reflections that contribute to the waveform (Liu *et al* 2013), while other works favor a five-kernel model (Couceiro *et al* 2015). The algorithms consisting of two kernels used in this work are shown to be robust against noise. The drawback is that all reflections are condensed in a single kernel, which rules out the possibility of assessing the relationship between the systolic component and specific reflections.

Another problem of the decomposition of the PPGI recordings is the morphology of the signals, which in some cases differs substantially from the usual PPG waveform. Algorithms with more than two kernels tend to adapt to these distortions. This overfitting leads to difficulties regarding the assessment of the second derivative as its characteristic morphology is thus changed. Algorithms with two kernels exhibited the best performance to retain this morphology. Thus, these algorithms showed the best denoising ability of the PWD algorithms, while retaining important morphological characteristics. This ability of the PWD algorithms has been proposed in the literature (Couceiro *et al* 2015, Lazaro *et al* 2018).

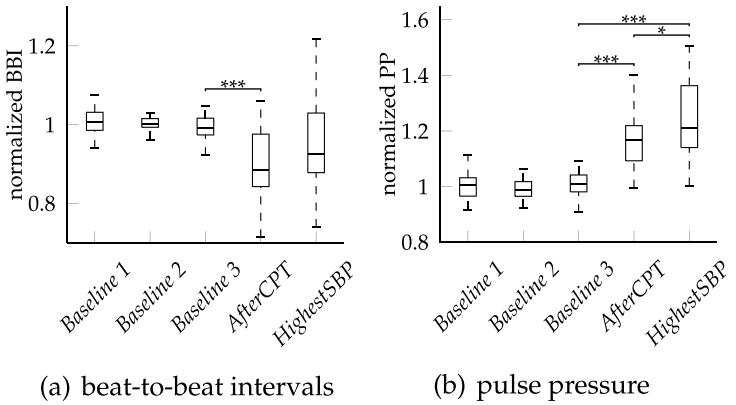

(a) beat-to-beat intervals (b) pulse pressure

Figure 10. Results of the assessment of the reference parameters of the CPT dataset, depicted by boxplots. If significant, post-hoc test outcomes are denoted by * $p < 0.05$, ** $p < 0.01$, *** $p < 0.001$. Outliers are not shown. All values are normalized to the mean of the three baseline analysis intervals.

Our results showed a statistically significant increase in *b*/*a* for the GammaGauss2generic algorithm (see figure 9(e)). A highly significant change in PP from our data could be observed (see figure 10(b)). The increase in PP can be explained by the pain stimulus of the CPT that triggers a sympathetic response.

These results indicate a relationship between *b*/*a* and PP and thus support the findings from the literature. The *b*/*a* ratio has been shown to be positively correlated with age (Takazawa *et al* 1998, Otsuka *et al* 2006, Baek *et al* 2007), systolic blood pressure and pulse pressure (Otsuka *et al* 2006). Some works reported a negative correlation between the absolute of *b*/*a* and these physiological measures (Imanaga *et al* 1998, Hashimoto *et al* 2002). As *b*/*a* is modulated by the early systolic phase, it is thought to be mainly influenced by the peripheral vessels (Imanaga *et al* 1998).

The decrease in T_{sysdia}, which is directly derived from the decomposition, however, could be seen in each of the four decomposition algorithms. The increased sympathetic tone is accompanied by a decrease in the length of the beat-to-beat intervals (see figure 10(a)). This leads to the expected shortened temporal difference between the systolic and diastolic components.

The temporal differences of kernels from PWD have been associated with blood pressure. Goswami *et al* (2010) reported a lowered temporal difference between the systolic and diastolic peaks, while most other works found a positive correlation between various blood pressure and temporal difference measures. Only Baruch *et al* (2011) considered the influence of heart rate on the temporal difference of the kernels and also showed a positive correlation to the length of the beat-to-beat intervals. We cannot rule out the possibility of blood pressure influencing T_{sysdia}.

The fact that only the decomposition with two kernels showed a significant change in *b*/*a* and only the Gamma3generic algorithm showed a similar trend further indicates the denoising ability of algorithms with a low number of kernels.

In order to reduce motion artifacts in PPGI signals, and thus possibly enhance the performance of the PWD algorithms, color channels can be combined. Wang *et al* (2017a) showed methods for channel combination like CHROM or POS to be beneficial for heart rate estimation. However, such methods affect the beat morphology and were not considered within this work. Instead, we analyzed the decomposition of the difference between the green and the red channel. The difference is hoped to eliminate general artifacts but leave the signal morphology, which is dominated by the green channel, undistorted. The results show the same trends as in the original green channel analysis. However, there are no statistically significant differences between the analysis intervals. The low signal quality of the red channel is likely to introduce noise into the combined signal and thus affect the signal morphology.

5.3. Limitations

Although this work demonstrates the general feasibility of PWD in PPGI, it has some limitations. The exclusion of 10 out of 43 recordings for the reasons explained in section 3.6 should be noted. This shows that, because of the limitations of the measurement system, not every recording is usable for PWD. The simulation also indicates that although PWD can be applied to denoise the PPG waveform, below a certain SNR, no PWD algorithm can reliably decompose the signal.

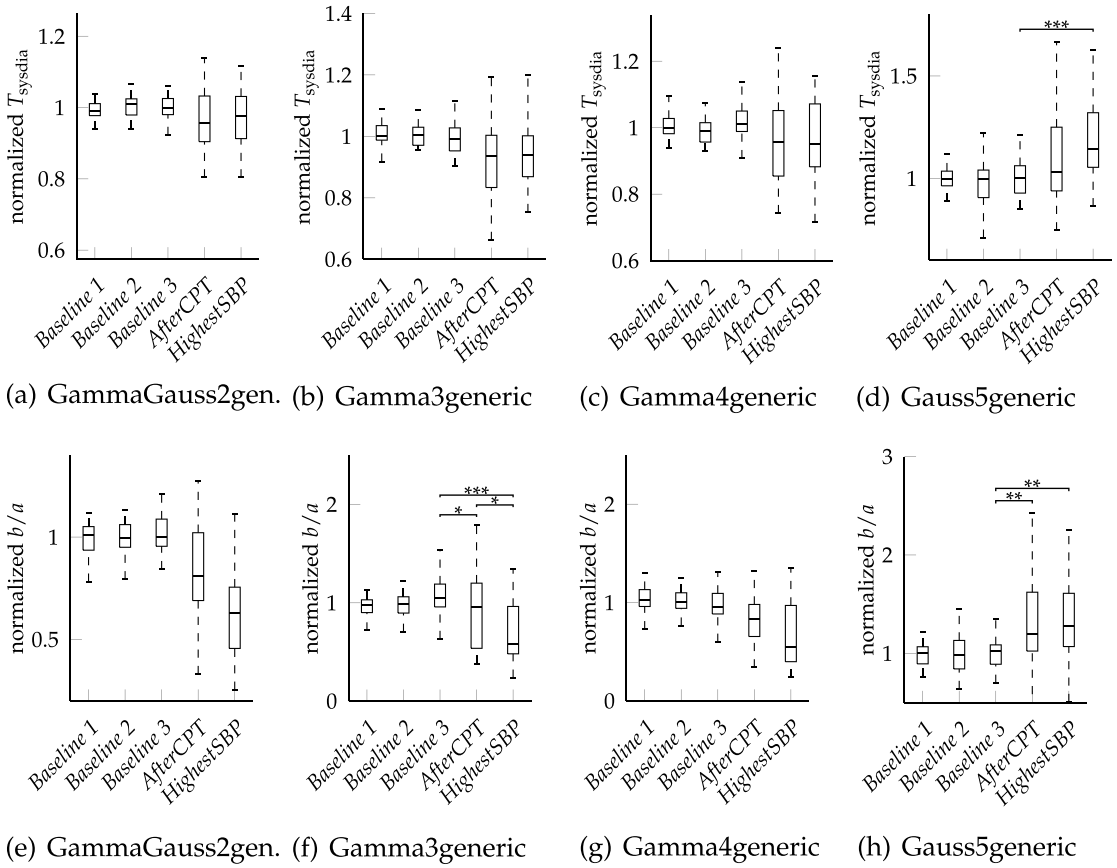

Figure 11. Results of the assessment of the CPT dataset's finger PPG data, depicted by boxplots. If significant, post-hoc test outcomes are denoted by * $p < 0.05$, ** $p < 0.01$, *** $p < 0.001$. Outliers are not shown. All values are normalized to the mean of the three baseline analysis intervals.

6. Conclusion and outlook

This work studied the applicability of PWD for analyzing the PPGI waveform. In summary, our investigations confirm the applicability of PWD particularly for a low number of kernels. This finding opens up novel possibilities for PPGI usage beyond heart rate monitoring. Our results further underline the importance of initial values and boundary conditions of PWD algorithms, which are often neglected.

We also analyzed the decomposition parameters on the finger PPG data (see figure 11). The results for b/a exhibit opposing trends for PPG and PPGI. The T_{sysdia} parameter, however, shows similar trends between PPGI and the finger PPG with the exception of Gauss5generic, which we consider the least robust of the PWD methods. We reported a similar phenomenon for the AC part of the ensemble beats (Fleischhauer *et al* 2019). Future work will explore the differences between finger PPG and PPGI in more detail.

In order to allow other researchers easy comparison of their own algorithms with previously published solutions and to foster further research on the topic, we have released the used algorithms and simulated data under the MIT license at https://github.com/FHDO-LAMBDA/PulseDecompositionAnalysis.

Acknowledgment

The authors want to thank the Deutsche Forschungsgemeinschaft (DFG, German Research Foundation) - Grant No. 401786308 for funding this work.

Appendix A. PWD parameters

This section lists PWD parameters and their calculation based on the pulse waves y, kernels g and parameter vectors θ of the kernels.

Augmentation index (AuI). The AuI is calculated differently depending on the type of pulse (Rubins 2008):

$$\mathrm{AuI} = 1 - \frac{y(\mu_1)}{y_{\max}} \qquad \text{typeA}, \tag{12}$$

$$\mathrm{AuI} = \frac{y(\mu_2)}{y_{\max}} - 1 \qquad \text{typeC}.$$

Reflection index (RI). The RI is usually calculated as the ratio of the diastolic and systolic amplitudes of the pulse wave (Goswami *et al* 2010, Couceiro *et al* 2015):

$$\mathrm{RI} = \frac{y_{\mathrm{dias}}}{y_{\mathrm{sys}}}. \tag{13}$$

Sorelli *et al* (2018) modified the RI as the percentage of ratios of the areas A beneath the diastolic and systolic pulse models:

$$\mathrm{RI} = 100\% \cdot \frac{A_{\mathrm{dias}}}{A_{\mathrm{sys}}}. \tag{14}$$

Another method for obtaining the RI can be found in the work of Rubins (2008):

$$\mathrm{RI} = \frac{y(\mu_3)}{y_{\max}}. \tag{15}$$

Crest time (CT). The CT is the duration of the pulse ascent and is measured as the time from the beginning of the pulse to the first zero crossing of the first derivative of the pulse wave (Sorelli *et al* 2018).

Stiffness index (SI). The SI is the difference in time of the position of the diastolic part of the pulse wave and the systolic part (Couceiro *et al* 2015, Sorelli *et al* 2018).

Foot-to-foot delay (D). D is the time between the onset of the forward and delayed pulses (Goswami *et al* 2010).

Differential pulse spread (DPS). The DPS is the difference between the standard deviations of the reflected pulse wave σ_{r} and the forward pulse wave σ_{f} (Goswami *et al* 2010):

$$\mathrm{DPS} = \sigma_{\mathrm{r}} - \sigma_{\mathrm{f}}. \tag{16}$$

Time differences (T1k). The most commonly used features are the time differences between the k-th kernel and the first kernel (Goswami *et al* 2010, Baruch *et al* 2011, Baruch *et al* 2014, Liu *et al* 2014, Couceiro *et al* 2015, Banerjee *et al* 2017, Lazaro *et al* 2018, Sorelli *et al* 2018, Wang *et al* 2018, Sorelli *et al* 2019):

$$\mathrm{T1k} = \mu_k - \mu_1. \tag{17}$$

Amplitude ratios (PkP1). Another very common feature is the ratio of the amplitude of the k-th kernel to the amplitude of the first kernel (Baruch *et al* 2014, Liu *et al* 2014, Sorelli *et al* 2018, Wang *et al* 2018):

$$\mathrm{PkP1} = \frac{g_{k\max}}{g_{1\max}}. \tag{18}$$

Appendix B. Motion artifacts

The motion artifacts z consist of the sum of two components: a linear trend z_{trend} and an impulse z_{impulse}. Such noise types have been observed experimentally in PPGI data upon slower or more abrupt movements. The linear trend can be written as

$$z_{\mathrm{trend}} = m \cdot t \tag{19}$$

with m being the slope of the line and t the time. The impulse can take two possible shapes randomly. One is a bell-shaped algebraic function:

$$z_{\text{impulse}}(t) = \frac{a}{1 + \left(\frac{t-\mu}{\sigma}^2\right)^{\frac{3}{2}}}. \tag{20}$$

The other is a windowed sinc function:

$$z_{\text{impulse}}(t) = \begin{cases} 0 & t > \mu + \pi \cdot \sigma \\ 0 & t < \mu - \pi \cdot \sigma \\ a \cdot \text{sinc}(\frac{t-\mu}{\sigma}) & \text{otherwise} \end{cases}, \tag{21}$$

where a is the amplitude, μ is the mean and σ a width parameter of the impulse. We also assigned random values to the orientation (positive or negative amplitude), the width parameter and the mean of the impulse. The mean can attain values in the interval:

$$\sigma \leq \mu \leq T - \sigma, \tag{22}$$

with T being the maximum of t. The width parameter is defined between:

$$\frac{T}{84 \cdot \sqrt{2\log 2}} \leq \sigma \leq \frac{4 \cdot T}{84 \cdot \sqrt{2\log 2}}. \tag{23}$$

These factors combined with the chosen SNR determine the absolute amplitude of the impulse.

Appendix C. Gamma kernel

As previously shown in the works of Tigges *et al* (2017a), we describe the Gamma kernel parameters (α, β, s) by using the mode m and the standard deviation σ of the kernel. This ensures better compatibility with the approaches that use *a priori* knowledge for finding the initial values and boundaries for the fitting of Gaussian kernels (Couceiro *et al* 2015, Sorelli *et al* 2018). Our formulation of the parameters differs from that of Tigges *et al* (2017a) in the dependence of α and β on m and σ. This section shows the derivation of our formulation of the Gamma kernels.

The mode m of a Gamma kernel $g(t)$ can be calculated from its first derivative:

$$\frac{dg(t)}{dt} = \frac{\beta^\alpha}{\Gamma(\alpha)} e^{-\beta t} t^{\alpha-1} \cdot \left(\frac{\alpha - 1}{t} - \beta \right). \tag{24}$$

m is t for which $\frac{dg(t)}{dt} \stackrel{!}{=} 0$ and can be expressed as

$$m = \frac{\alpha - 1}{\beta}. \tag{25}$$

The amplitude parameter s is then chosen in such a way that $g(t = m)$ divided by s becomes a. In this way we get s from equation (4):

$$s = \frac{1}{b} \frac{\beta^\alpha}{\Gamma(\alpha)} \left(\frac{\alpha - 1}{\beta}\right)^{\alpha-1} e^{1-\alpha}. \tag{26}$$

The variance σ^2 of a Gamma kernel in terms of α and β is (Kroese and Chan 2014):

$$\sigma^2 = \frac{\alpha}{\beta^2}. \tag{27}$$

Equation (25) can be plugged into equation (27) to obtain our formulations of α and β:

$$\beta = \frac{1}{2\sigma^2} \left(m + \sqrt{m^2 + 4\sigma^2} \right), \tag{28}$$

$$\alpha = \frac{1}{2\sigma^2} \left(m^2 + m\sqrt{m^2 + 4\sigma^2} \right) + 1. \tag{29}$$

Appendix D. Model optimization parameters

This sections lists the initial values and boundaries of the optimization parameters of the used algorithms for a PPG signal in the range of $[0, \text{PPG}_{\text{max}}]$ with its starting point at $t = 0$ s and its ending point at $t = T$.

Table D1. List of the initial values and boundaries (lower boundary *lb*, upper boundary *ub*) for the *k* kernels of the applied PWD algorithms that use five Gaussian kernels.

Algorithm	*k*	Parameter	*lb*	Initial value	*ub*
Couceiro	1	Amplitude	$0.5 \cdot \mathrm{PPG}(t_\mathrm{a})$	$0.7 \cdot \mathrm{PPG}(t_\mathrm{a})$	$\mathrm{PPG}(t_\mathrm{b})$
		Mean	t_a [(1)]	t_a	t_b [(2)]
		Standard Deviation	0 s	$t_\mathrm{a}/3$	$t_\mathrm{b}/3$
	2	Amplitude	$0.5 \cdot \mathrm{PPG}_\mathrm{sys}$ [(3)]	$0.9 \cdot \mathrm{PPG}_\mathrm{sys}$	$\mathrm{PPG}_\mathrm{sys}$
		Mean	t_a	t_b	t_c [(4)]
		Standard Deviation	$t_\mathrm{a}/3$	$t_\mathrm{b}/3$	$t_\mathrm{d}/3$
	3	Amplitude	$0.2 \cdot \mathrm{PPG}_\mathrm{sys}$	$0.5 \cdot \mathrm{PPG}_\mathrm{sys}$	$0.8 \cdot \mathrm{PPG}_\mathrm{sys}$
		Mean	t_b	t_d [(5)]	t_dn1 [(6)]
		Standard Deviation	$t_\mathrm{b}/3$	$t_\mathrm{d}/3$	$t_\mathrm{dn1}/3$
	4	Amplitude	0 s	$0.8 \cdot \mathrm{PPG}_\mathrm{dia}$ [(7)]	$\mathrm{PPG}_\mathrm{dia}$
		Mean	t_dn2 [(8)]	t_f [(9)]	T
		Standard Deviation	0 s	$\min(t_f, (T - t_f)/3)$	t_dn2
	5	Amplitude	0 s	$0.3 \cdot \mathrm{PPG}_\mathrm{dia}$	$\mathrm{PPG}_\mathrm{dia}$
		Mean	t_f	t_dia [(10)]	T
		Standard Deviation	0 s	$T - \overline{(T - t_f)}$	t_dn2
Generic	1	Amplitude	0 s	$0.8 \cdot \mathrm{PPG}_\mathrm{max}$	$\mathrm{PPG}_\mathrm{max}$
		Mean	0 s	$(2/7) \cdot T$	T
		Standard Deviation	0 s	$((2/7) \cdot T) \cdot (2\sqrt{2\log 2})^{-1}$	T
	2	Amplitude	0 s	$0.3 \cdot \mathrm{PPG}_\mathrm{max}$	$\mathrm{PPG}_\mathrm{max}$
		Mean	0 s	$(3/7) \cdot T$	T
		Standard Deviation	0 s	$((1/7) \cdot T) \cdot (2\sqrt{2\log 2})^{-1}$	T
	3	Amplitude	0 s	$0.3 \cdot \mathrm{PPG}_\mathrm{max}$	$\mathrm{PPG}_\mathrm{max}$
		Mean	0 s	$(4/7) \cdot T$	T
		Standard Deviation	0 s	$((1/7) \cdot T) \cdot (2\sqrt{2\log 2})^{-1}$	T
	4	Amplitude	0 s	$0.3 \cdot \mathrm{PPG}_\mathrm{max}$	$\mathrm{PPG}_\mathrm{max}$
		Mean	0 s	$(5/7) \cdot T$	T
		Standard Deviation	0 s	$((1/7) \cdot T) \cdot (2\sqrt{2\log 2})^{-1}$	T
	5	Amplitude	0 s	$0.3 \cdot \mathrm{PPG}_\mathrm{max}$	$\mathrm{PPG}_\mathrm{max}$
		Mean	0 s	$(6/7) \cdot T$	T
		Standard Deviation	0 s	$((1/7) \cdot T) \cdot (2\sqrt{2\log 2})^{-1}$	T

(1) time of the maximum of the *a* wave of the second derivative of the PPG
(2) time of the maximum of the *b* wave of the second derivative of the PPG
(3) $\mathrm{PPG}_\mathrm{sys} = \max([\mathrm{PPG}(t_\mathrm{b}), \mathrm{PPG}(t_\mathrm{c}), \mathrm{PPG}(t_\mathrm{d})])$
(4) time of the maximum of the *c* wave of the second derivative of the PPG
(5) time of the maximum of the *d* wave of the second derivative of the PPG
(6) time of the left boundary of the dicrotic notch
(7) $\mathrm{PPG}_\mathrm{dia} = \max([\mathrm{PPG}(t_\mathrm{dn1}), \ldots, \mathrm{PPG}(T)])$
(8) time of the right boundary of the dicrotic notch
(9) time of the maximum of the *f* wave of the second derivative of the PPG
(10) $t_\mathrm{dia} = t(\mathrm{PPG}_\mathrm{dia})$

Table D2. List of the initial values and boundaries (lower boundary *lb*, upper boundary *ub*) for the *k* kernels of the algorithm of Sorelli *et al* (2018). This applies to Gamma, Gaussian and GammaGaussian kernels.

Algorithm	*k*	Parameter	*lb*	Initial value	*ub*
2 kernels	1	Amplitude	$0.5 \cdot \mathrm{PPG_{max}}$	$0.8 \cdot \mathrm{PPG_{max}}$	$\mathrm{PPG_{max}}$
		Mean	0 s	$0.5 \cdot \Delta t_{sys}$ [(1)]	t_{inc} [(2)]
		Standard Deviation	$0.5 \cdot \Delta t_{sys} \cdot (2\sqrt{2\log 2})^{-1}$	$\Delta t_{sys} \cdot (2\sqrt{2\log 2})^{-1}$	$1.5 \cdot \Delta t_{sys} \cdot (2\sqrt{2\log 2})^{-1}$
	2	Amplitude	0 s	$0.4 \cdot \mathrm{PPG_{max}}$	$0.6 \cdot \mathrm{PPG_{max}}$
		Mean	t_{inc}	$t_{inc} + 0.33 \cdot \Delta t_{dia}$ [(3)]	T
		Standard Deviation	$0.3 \cdot \Delta t_{dia} \cdot (2\sqrt{2\log 2})^{-1}$	$0.75 \cdot \Delta t_{dia} \cdot (2\sqrt{2\log 2})^{-1}$	$\Delta t_{dia} \cdot (2\sqrt{2\log 2})^{-1}$
3 kernels	1	Amplitude	$0.5 \cdot \mathrm{PPG_{max}}$	$0.8 \cdot \mathrm{PPG_{max}}$	$\mathrm{PPG_{max}}$
		Mean	0 s	$0.5 \cdot \Delta t_{sys}$	t_{inc}
		Standard Deviation	$0.5 \cdot \Delta t_{sys} \cdot (2\sqrt{2\log 2})^{-1}$	$\Delta t_{sys} \cdot (2\sqrt{2\log 2})^{-1}$	$1.5 \cdot \Delta t_{sys} \cdot (2\sqrt{2\log 2})^{-1}$
	2	Amplitude	0 s	$0.4 \cdot \mathrm{PPG_{max}}$	$0.6 \cdot \mathrm{PPG_{max}}$
		Mean	t_{inc}	$t_{inc} + 0.167 \cdot \Delta t_{dia}$	T
		Standard Deviation	$0.15 \cdot \Delta t_{dia} \cdot (2\sqrt{2\log 2})^{-1}$	$0.375 \cdot \Delta t_{dia} \cdot (2\sqrt{2\log 2})^{-1}$	$0.5 \cdot \Delta t_{dia} \cdot (2\sqrt{2\log 2})^{-1}$
	3	Amplitude	0 s	$0.4 \cdot \mathrm{PPG_{max}}$	$0.6 \cdot \mathrm{PPG_{max}}$
		Mean	t_{inc}	$t_{inc} + 0.5 \cdot \Delta t_{dia}$	T
		Standard Deviation	$0.15 \cdot \Delta t_{dia} \cdot (2\sqrt{2\log 2})^{-1}$	$0.375 \cdot \Delta t_{dia} \cdot (2\sqrt{2\log 2})^{-1}$	$0.5 \cdot \Delta t_{dia} \cdot (2\sqrt{2\log 2})^{-1}$
4 kernels	1	Amplitude	$0.5 \cdot \mathrm{PPG_{max}}$	$0.8 \cdot \mathrm{PPG_{max}}$	$\mathrm{PPG_{max}}$
		Mean	0 s	$0.5 \cdot \Delta t_{sys}$	t_{inc}
		Standard Deviation	$0.5 \cdot \Delta t_{sys} \cdot (2\sqrt{2\log 2})^{-1}$	$\Delta t_{sys} \cdot (2\sqrt{2\log 2})^{-1}$	$1.5 \cdot \Delta t_{sys} \cdot (2\sqrt{2\log 2})^{-1}$
	2	Amplitude	0 s	$0.4 \cdot \mathrm{PPG_{max}}$	$0.6 \cdot \mathrm{PPG_{max}}$
		Mean	t_{inc}	t_{inc}	T
		Standard Deviation	$0.1 \cdot \Delta t_{dia} \cdot (2\sqrt{2\log 2})^{-1}$	$0.25 \cdot \Delta t_{dia} \cdot (2\sqrt{2\log 2})^{-1}$	$0.33 \cdot \Delta t_{dia} \cdot (2\sqrt{2\log 2})^{-1}$
	3	Amplitude	0 s	$0.4 \cdot \mathrm{PPG_{max}}$	$0.6 \cdot \mathrm{PPG_{max}}$
		Mean	t_{inc}	$t_{inc} + 0.33 \cdot \Delta t_{dia}$	T
		Standard Deviation	$0.1 \cdot \Delta t_{dia} \cdot (2\sqrt{2\log 2})^{-1}$	$0.25 \cdot \Delta t_{dia} \cdot (2\sqrt{2\log 2})^{-1}$	$0.33 \cdot \Delta t_{dia} \cdot (2\sqrt{2\log 2})^{-1}$
	4	Amplitude	0 s	$0.4 \cdot \mathrm{PPG_{max}}$	$0.6 \cdot \mathrm{PPG_{max}}$
		Mean	t_{inc}	$t_{inc} + 0.67 \cdot \Delta t_{dia}$	T
		Standard Deviation	$0.1 \cdot \Delta t_{dia} \cdot (2\sqrt{2\log 2})^{-1}$	$0.25 \cdot \Delta t_{dia} \cdot (2\sqrt{2\log 2})^{-1}$	$0.33 \cdot \Delta t_{dia} \cdot (2\sqrt{2\log 2})^{-1}$

[(1)] time span between starting point of the PPG pulse and the incisura

[(2)] time of the incisura

[(3)] time span between the incisura and the ending point of the PPG pulse

Table D3. List of the initial values and boundaries (lower boundary *lb*, upper boundary *ub*) for the *k* kernels of the applied PWD algorithms that use generic initial values. This applies to Gamma, Gaussian and GammaGaussian kernels.

Algorithm	*k*	Parameter	*lb*	Initial value	*ub*
2 kernels	1	Amplitude	0 s	$0.8 \cdot \mathrm{PPG}_{\max}$	$\mathrm{PPG}_{\max}$
		Mean	0 s	$(2/7) \cdot T$	T
		Standard Deviation	0 s	$((2/7) \cdot T) \cdot (2\sqrt{2\log 2})^{-1}$	T
	2	Amplitude	0 s	$0.5 \cdot \mathrm{PPG}_{\max}$	$\mathrm{PPG}_{\max}$
		Mean	0 s	$(4/7) \cdot T$	T
		Standard Deviation	0 s	$((3/7) \cdot T) \cdot (2\sqrt{2\log 2})^{-1}$	T
3 kernels	1	Amplitude	0 s	$0.8 \cdot \mathrm{PPG}_{\max}$	$\mathrm{PPG}_{\max}$
		Mean	0 s	$(2/7) \cdot T$	T
		Standard Deviation	0 s	$((2/7) \cdot T) \cdot (2\sqrt{2\log 2})^{-1}$	T
	2	Amplitude	0 s	$0.4 \cdot \mathrm{PPG}_{\max}$	$\mathrm{PPG}_{\max}$
		Mean	0 s	$(4/7) \cdot T$	T
		Standard Deviation	0 s	$((2/7) \cdot T) \cdot (2\sqrt{2\log 2})^{-1}$	T
	3	Amplitude	0 s	$0.2 \cdot \mathrm{PPG}_{\max}$	$\mathrm{PPG}_{\max}$
		Mean	0 s	$(5/7) \cdot T$	T
		Standard Deviation	0 s	$((2/7) \cdot T) \cdot (2\sqrt{2\log 2})^{-1}$	T
4 kernels	1	Amplitude	0 s	$0.8 \cdot \mathrm{PPG}_{\max}$	$\mathrm{PPG}_{\max}$
		Mean	0 s	$(2/7) \cdot T$	T
		Standard Deviation	0 s	$((2/7) \cdot T) \cdot (2\sqrt{2\log 2})^{-1}$	T
	2	Amplitude	0 s	$0.4 \cdot \mathrm{PPG}_{\max}$	$\mathrm{PPG}_{\max}$
		Mean	0 s	$(3/7) \cdot T$	T
		Standard Deviation	0 s	$((2/7) \cdot T) \cdot (2\sqrt{2\log 2})^{-1}$	T
	3	Amplitude	0 s	$0.4 \cdot \mathrm{PPG}_{\max}$	$\mathrm{PPG}_{\max}$
		Mean	0 s	$(1/2) \cdot T$	T
		Standard Deviation	0 s	$((2/7) \cdot T) \cdot (2\sqrt{2\log 2})^{-1}$	T
	4	Amplitude	0 s	$0.4 \cdot \mathrm{PPG}_{\max}$	$\mathrm{PPG}_{\max}$
		Mean	0 s	$(45/70) \cdot T$	T
		Standard Deviation	0 s	$((2/7) \cdot T) \cdot (2\sqrt{2\log 2})^{-1}$	T

ORCID iD

Sebastian Zaunseder https://orcid.org/0000-0001-6114-3142

References

Allen J 2007 Photoplethysmography and its application in clinical physiological measurement *Physiol. Meas.* **28** 1–39

Awad A A, Ghobashy M A M, Ouda W, Stout R G, Silverman D G and Shelley K H 2001 Different responses of ear and finger pulse oximeter wave form to cold pressor test *Anesth. Analg.* **92** 1483–6

Baek H J, Kim J S, Kim Y S, Lee H B and Park K S 2007 Second derivative of photoplethysmography for estimating vascular aging *2007 6th Int. Special Conf. on Information Technology Applications in Biomedicine* IEEE vol 893 pp 70–2

Banerjee S, Bailón R, Lazáro J, Marozas V, Laguna P and Gil E 2017 A two step Gaussian modelling to assess PPG morphological variability induced by psychological stress *Comput. Cardiol.* **44** 1–4

Baruch M C, Kalantari K, Gerdt D W and Adkins C M 2014 Validation of the pulse decomposition analysis algorithm using central arterial blood pressure *Biomed. Eng. Online* **13** 1–19

Baruch M C, Warburton D E, Bredin S S, Cote A, Gerdt D W and Adkins C M 2011 Pulse decomposition analysis of the digital arterial pulse during hemorrhage simulation *Nonlinear Biomed. Phys.* **5** 1–15

Bortolotto L A, Blacher J, Kondo T, Takazawa K and Safar M E 2000 Assessment of vascular aging and atherosclerosis in hypertensive subjects: Second derivative of photoplethysmogram versus pulse wave velocity *Am. J. Hypertension* **13** 165–71

Budidha K and Kyriacou P A 2019 Photoplethysmography for quantitative assessment of sympathetic nerve activity (SNA) during cold stress *Front. Physiol.* **10** 1–10

Chellappan K, Mohd Ali M A and Zahedi E 2008 An age index for vascular system based on photoplethysmogram pulse contour analysis *4th Kuala Lumpur Int. Conf. on Biomedical Engineering 2008* (*Berlin, Heidelberg*) vol 21 pp 125–8

Couceiro R *et al* 2015 Assessment of cardiovascular function from multi-Gaussian fitting of a finger photoplethysmogram *Physiol. Meas.* **36** 1801–25

Couceiro R, Carvalho P, Paiva R P, Henriques J, Antunes M, Quintal I and Muehlsteff J 2012 Multi-Gaussian fitting for the assessment of left ventricular ejection time from the photoplethysmogram *Proc. Annual Int. Conf. IEEE Engineering in Medicine and Biology Society, EMBS* pp 3951–4

Dawber T R, Thomas H E and McNamara P M 1973 Characteristics of the dicrotic notch of the arterial pilse wave in coronary heart disease *Angiology* **24** 244–55

Djeldjli D, Bousefsaf F, Maaoui C and Bereksi-Reguig F 2019 Imaging photoplethysmography: signal waveform analysis *Proc. 2019 10th IEEE Int. Conf. on Intelligent Data Acquisition and Advanced Computing Systems: Technology and Applications, IDAACS 2019* vol 2 pp 830–4

Elgendi M, Jonkman M and Deboer F 2010 Heart rate variability measurement using the second derivative photoplethysmogram *Proc. Third Int. Conf. on Bio-Inspired Systems and Signal Processing* pp 82–7

Elgendi M 2012 On the analysis of fingertip photoplethysmogram signals *Current Cardiol. Rev.* **8** 14–25

Fleischhauer V, Woyczyk A, Rasche S and Zaunseder S 2019 Impact of sympathetic activation in imaging photoplethysmography *IEEE Int. Conf. on Computer Vision (ICCV) Workshops*

Goswami D, Chaudhuri K and Mukherjee J 2010 A new two-pulse synthesis model for digital volume pulse signal analysis *Cardiovasc. Eng.* **10** 109–17

Hashimoto J *et al* 2002 Pulse wave velocity and the second derivative of the finger photoplethysmogram in treated hypertensive patients: Their relationship and associating factors *J. Hypertension* **20** 2415–22

Holm S 1979 A simple sequential rejective method procedure *Scandinavian J. Stat.* **6** 65–70

Huang S-C, Jan H-Y, Lin W-C, Tsia C-L and Lin K-P 2015 Evaluation of decomposition analysis on multi-models for digital volume pulse signal *IFMBE Proc.* **51** 1731–4

Huelsbusch M and Blazek V 2002 Contactless mapping of rhythmical phenomena in tissue perfusion using PPGI *Proc. SPIE 4683, Medical Imaging 2002: Physiology and Function From Multidimensional Images* pp 110–7

Huotari M, Vehkaoja A, Määttä K and Kostamovaara J 2011 Photoplethysmography and its detailed pulse waveform analysis for arterial stiffness *J. Struct. Mech.* **44** 345–62

Iketani Y, Iketani T, Takazawa K and Murata M 2000 Second derivative of photoplethysmogram in children and young people *Jpn. Circ. J.* **64** 110–6

Imanaga I, Hara H, Koyanagi S and Tanaka K 1998 Correlation between wave components of the second derivative of plethysmogram and arterial distensibility *Jpn. Heart J.* **39** 775–84

Inuma J, Murakoshi M, Kobayashi T, Io H, Kaneko K, Takahashi T, Hamada C, Horikoshi S and Tomino Y 2012 Relationship between acceleration plethysmography and aortic calcification index in chronic kidney disease patients *Hong Kong J. Nephrol.* **14** 48–53

Jaryal A K, Selvaraj N, Santhosh J, Anand S and Deepak K K 2009 Monitoring of cardiovascular reactivity to cold stress using digital volume pulse characteristics in health and diabetes *J. Clinical Monitoring Comput.* **23** 123–30

Kamshilin A A, Zaytsev V V and Mamontov O V 2017 Novel contactless approach for assessment of venous occlusion plethysmography by video recordings at the green illumination *Sci. Rep.* **7** 1–9

Kroese D P and Chan J C C 2014 *Statistical Modeling and Computation* (Berlin: Springer)

Lazaro J E, Vergara J M and Laguna P 2014 Pulse rate variability analysis for discrimination of sleep-apnea-related decreases in the amplitude fluctuations of pulse photoplethysmographic signal in children *IEEE J. Biomed. Health Informatics* **18** 240–6

Lazaro J, Kontaxis S, Bailon R, Laguna P and Gil E 2018 Respiratory rate derived from pulse photoplethysmographic signal by pulse decomposition analysis *Proc. Annual Int. Conf. IEEE Engineering in Medicine and Biology Society, EMBS Jul 2018* pp 5282–5

Liu C, Zhao L and Liu C 2014 Effects of blood pressure and sex on the change of wave reflection: Evidence from Gaussian fitting method for radial artery pressure waveform *PLoS ONE* **9** 1–7

Liu C, Zheng D, Murray A and Liu C 2013 Modeling carotid and radial artery pulse pressure waveforms by curve fitting with Gaussian functions *Biomed. Signal Process. Control* **8** 449–54

López-Beltrán E A, Blackshear P L, Finkelstein S M and Cohn J N 1998 Non-invasive studies of peripheral vascular compliance using a non-occluding photoplethysmographic method *Med. Biol. Eng. Comput.* **36** 748–53

Miyai N, Miyashita K, Arita M, Morioka I, Kamiya K and Takeda S 2001 Noninvasive assessment of arterial distensibility in adolescents using the second derivative of photoplethysmogram waveform *Eur. J. Appl. Physiol.* **86** 119–24

Nishidate I, Tanabe C, McDuff D J, Nakano K, Niizeki K, Aizu Y and Haneishi H 2019 RGB camera-based noncontact imaging of plethysmogram and spontaneous low-frequency oscillation in skin perfusion before and during psychological stress *Optical Diagnostics and Sensing XIX: Toward Point-of-Care Diagnostics* ed G L Coé (Washington: SPIE) vol 1088507 p 7

Njoum H and Kyriacou P A 2013 Investigation of finger reflectance photoplethysmography in volunteers undergoing a local sympathetic stimulation *J. Physics: Conf. Series* **450**

Otsuka T, Kawada T, Katsumata M and Ibuki C 2006 Utility of second derivative of the finger photoplethysmogram for the estimation of the risk of coronary heart disease in the general population *Circ. J.* **70** 304–10

Padilla J M, Berjano E J, Sáiz J, Rodriguez R and Fácila L 2009 Pulse wave velocity and digital volume pulse as indirect estimators of blood pressure: Pilot study on healthy volunteers *Cardiovasc. Eng.* **9** 104–12

Paul M, Yu X, Wu B, Weiss C, Antink C H, Blazek V and Leonhardt S 2019 Waveform analysis for camera-based photoplethysmography imaging *Proc. Annual Int. Conf. IEEE Engineering in Medicine and Biology Society, EMBS* pp 2713–8

Rubins U 2008 Finger and ear photoplethysmogram waveform analysis by fitting with Gaussians *Med. Biol. Eng. Comput.* **46** 1271–6

Skoluda N *et al* 2015 Intra-individual psychological and physiological responses to acute laboratory stressors of different intensity *Psychoneuroendocrinology* **51** 227–36

Sorelli M, Kopietz C, Zaunseder S and Bocchi L 2019 Pulse decomposition analysis in camera-based photoplethysmography *2019 41st Annual Int. Conf. IEEE Engineering in Medicine and Biology Society (EMBC)* pp 3179–82

Sorelli M, Perrella A and Bocchi L 2018 Detecting vascular age using the analysis of peripheral pulse *IEEE Trans. Biomed. Eng.* **65** 2742–50

Takazawa K, Tanaka N, Fujita M, Matsuoka O, Saiki T, Aikawa M, Tamura S and Ibukiyama C 1998 Assessment of vasoactive agents and vascular aging by the second derivative of photoplethysmogram waveform *Hypertension* **32** 365–70

Tigges T, Pielmuș A, Klum M, Feldheiser A, Hunsicker O and Orglmeister R 2017b Model selection for the pulse decomposition analysis of fingertip photoplethysmograms *Proc. Annual Int. Conf. IEEE Engineering in Medicine and Biology Society, EMBS* pp 4014–7

Tigges T, Rockstroh J, Pielmuș A, Klum M, Feldheiser A, Hunsicker O and Orglmeister R 2017a In-ear photoplethysmography for central pulse waveform analysis in non-invasive hemodynamic monitoring *Current Directions Biomed. Eng.* **3** 587–90

Trumpp A, Bauer P L, Rasche S, Malberg H and Zaunseder S 2017 The value of polarization in camera-based photoplethysmography *Biomed. Opt. Express* **8** 2822–34

Trumpp A, Schell J, Malberg H and Zaunseder S 2016 Vasomotor assessment by camera-based photoplethysmography *Current Directions Biomed. Eng.* **2** 199–202

Verkruysse W, Svaasand L O and Nelson J 2008 Remote plethysmographic imaging using ambient light *Opt. Express* **16** 21434–45

Wang A, Yang L, Wen W, Zhang S, Gu G and Zheng D 2018 Gaussian modelling characteristics changes derived from finger photoplethysmographic pulses during exercise and recovery *Microvascular Res.* **116** 20–5

Wang L, Pickwell-MacPherson E, Liang Y and Zhang Y 2009 Noninvasive cardiac output estimation using a novel photoplethysmogram index *2009 Annual Int. Conf. IEEE Engineering in Medicine and Biology Society* IEEE pp 1746–9

Wang L, Xu L, Feng S, Meng M Q and Wang K 2013 Multi-Gaussian fitting for pulse waveform using weighted least squares and multi-criteria decision making method *Comput. Biol. Med.* **43** 1661–72

Wang W, Den Brinker A C, Stuijk S and De Haan G 2017 Robust heart rate from fitness videos *Physiol. Meas.* **38** 1023–44

Weiß C 2013 *Basiswissen Medizinische Statistik* (Berlin: Springer)

Xing X, Ma Z, Zhang M, Zhou Y, Dong W and Song M 2019 An unobtrusive and calibration-free blood pressure estimation method using photoplethysmography and biometrics *Sci. Rep.* **9** 1–8

Zaunseder S, Trumpp A, Wedekind D and Malberg H 2018b Cardiovascular assessment by imaging photoplethysmography – a review *Biomed. Tech.* **63** 1–18